energies

MDPI

Article

Hybrid Wind-Solar Power System with a Battery-Assisted Quasi-Z-Source Inverter: Optimal Power Generation by Deploying Minimum Sensors

Matija Bubalo, Mateo Bašić *, Dinko Vukadinović and Ivan Grgić

Department of Power Engineering, Faculty of Electrical Engineering, Mechanical Engineering and Naval Architecture, University of Split, 21000 Split, Croatia

* Correspondence: mabasic@fesb.hr

Abstract: This paper presents a hybrid renewable energy system (RES) including wind and photovoltaic (PV) power sources. The wind energy subsystem (WES) consists of a squirrel-cage induction generator (SCIG) driven by a variable-speed wind turbine (WT) and corresponding power electronic converter, by means of which a speed-sensorless indirect-rotor-field-oriented control of the SCIG is implemented. The outputs of both the WES and PV power source rated 1.5 kW and 3.5 kW, respectively, are connected to the DC bus, with the quasi-Z-source inverter (qZSI) acting as an interlinking converter between the DC bus and the AC grid/load. An advanced pulse-width-modulation scheme is applied to reduce the qZSI switching losses. The considered RES can operate both in grid-tie and island operation, whereas the battery storage system—integrated within the qZSI impedance network—enables more efficient energy management. The proposed control scheme includes successively executed algorithms for the optimization of the WES and PV power outputs under varying atmospheric conditions. A perturb-and-observe PV optimization algorithm is executed first due to the significantly faster dynamics and higher-rated power of the PV source compared to the WES. The WES optimization algorithm includes two distinct fuzzy logic optimizations: one for extraction of the maximum wind power and the other for minimization of the SCIG losses. To reduce the number of the required sensors, all three MPPT algorithms utilize the same input variable—the qZSI's input power—thus increasing the system's reliability and reducing the cost of implementation. The performance of the proposed hybrid RES was experimentally evaluated over wide ranges of simulated atmospheric conditions in both the island and grid-tie operation.

Keywords: batteries; loss minimization; maximum power point tracking; photovoltaic source emulation; quasi-z-source inverter; wind turbine emulation

Citation: Bubalo, M.; Bašić, M.; Vukadinović, D.; Grgić, I. Hybrid Wind-Solar Power System with a Battery-Assisted Quasi-Z-Source Inverter: Optimal Power Generation by Deploying Minimum Sensors. *Energies* **2023**, *16*, 1488. https://doi.org/10.3390/en16031488

Academic Editors: Elyas Rakhshani, Aleksandra Lekić and Peter Palensky

Received: 23 December 2022
Revised: 25 January 2023
Accepted: 30 January 2023
Published: 2 February 2023

1. Introduction

Solar and wind energy are harnessed all over the world by means of photovoltaic (PV) panels and wind turbines (WTs), respectively. However, the power production of these sources is highly intermittent and unpredictable. The WT power output varies with respect to the wind speed, whereas the frequency and amplitude of the generated voltage vary with respect to the shaft speed and torque, respectively. Similarly, the PV panel power output varies with respect to solar irradiance and panel temperature. Hence, a control algorithm is needed to keep the WT and PV power output under control and additionally ensure maximum power extraction, with energy efficiency being crucial for the cost-effectiveness of renewable energy systems (RESs), especially small-scale.

The maximum power output of a variable-speed WT can be achieved by adjusting the shaft speed in accordance with the wind speed. The most commonly used maximum power point tracking (MPPT) algorithms for WTs are power signal feedback (PSF) algorithms [1,2], tip speed ratio (TSR) algorithms [3,4], and perturb and observe (P&O) algorithms [5,6]. PSF algorithms require measurement of the WT power or shaft speed and knowledge of the WT

maximum power curve, which may change with atmospheric conditions or WT aging. TSR algorithms require accurate measurement of both the shaft speed and wind speed, which can prove to be demanding. P&O algorithms, on the other hand, do not require wind speed measurement or prior knowledge of the WT characteristics; they only require feedback on how the previous perturbation of the control variable affected the WT output power, so the next perturbation is determined based on that information. The main disadvantage of P&O algorithms is their slower convergence, which can be compensated to a certain extent by the utilization of fuzzy logic (FL), artificial neural networks (ANN), or hedge algebra (HA) controllers. In [7], it was shown that this type of controller ensures a fast response of the WT shaft speed with short settling time and negligible overshoot in the whole WT operating range, which is something that the proportional-integral (PI) controller is not capable of. P&O algorithms are generally more suited for small-scale WTs, which have lower inertia and thus allow for shorter optimization time-step.

In small-scale wind energy conversion systems (WECSs), squirrel-cage induction generators (SCIGs) are regarded as an attractive alternative to permanent magnet synchronous generators (PMSGs) and doubly fed induction generators (DFIGs). PMSGs do not require external excitation and are easier to control, but they are more expensive than SCIGs, which is an important factor in low-power systems. In such systems, SCIGs offer several advantages over DFIGs, such as lower price, more rugged construction, fewer maintenance requirements, and higher efficiency. The SCIG can be self-excited by external excitation capacitors connected directly or via a power electronic converter. In addition, by implementing field-oriented control, decoupled control of the SCIG torque and magnetizing flux can be achieved. This feature enables both WT power optimization and SCIG loss minimization. In the case of indirect rotor-field-oriented (IRFO) control, the loss minimization is achieved through adjustment of the SCIG rotor flux reference. Loss-minimization algorithms reported in the literature can be classified into search-based [8,9] and model-based [6,10] algorithms. P&O algorithms, belonging to the first group, require only knowledge of the change in the SCIG power caused by the last imposed perturbation, but are characterized by slower convergence. Model-based algorithms are known to be somewhat faster, but they are inherently sensitive to machine parameter variations, with their efficiency being strongly dependable on the level of accuracy of the utilized SCIG model.

PV panels typically generate low-level DC voltage, so they are commonly combined with DC-DC boost-type converters. Moreover, in AC applications, a two-stage power conversion topology consisting of a DC-DC boost converter and a voltage-source inverter (VSI) is typically encountered [11,12]. The quasi-Z-source inverter (qZSI) represents an alternative, single-stage topology that enables both the boost and control of the PV source voltage, thus eliminating the DC-DC converter [13]. The voltage boost is achieved by means of an impedance network and the additional shoot-through (ST) switching state, which is implemented by short-circuiting the inverter bridge during the traditional zero-switching states. The qZSI also allows for battery integration without having to introduce additional semiconductor switches. The possibility of energy storage is extremely important for efficient energy management in RESs (e.g., for effective MPPT application in the island operation), with the batteries being commonly used for this purpose.

The P&O type MPPT algorithms are most commonly encountered in PV systems [14,15], which is due to their simple implementation. The convergence speed of these algorithms is much faster than in the case of the WT due to the comparably faster dynamics of the PV source. The implementation of a P&O algorithm in PV systems with the battery-assisted qZSI typically implies the measurement of the PV source voltage and current [16–21]. The MPPT proposed in [22], on the other hand, requires measurement of both the solar irradiance (Z) and PV panel temperature (T_{pv}), but the installation of additional measurement sensors increases the cost of implementation while decreasing the system's reliability. The MPPT algorithm proposed in [23] does not require any additional sensors

and utilizes a single fixed value of the qZSI ST duty ratio, but it is inherently susceptible to high tracking errors in the case of T_{pv} variations.

PV-fed qZSIs have been considered in many recent studies. In the grid-tie applications considered in [24,25], one of the main tasks of the control algorithm is to extract the maximum PV power and inject it into the grid. However, due to the absence of an energy storage system in [24,25], the island operation is not viable. Integration of the battery storage system not only enables the island operation with the maximum PV power, but it also enables peak shaving, voltage control support, oscillation damping as well as an extra degree of freedom in the grid-tie operation. In the qZSI, the batteries are typically connected in parallel with the higher-voltage capacitor, as in [26,27], or in parallel with the lower-voltage capacitor, as in [16–23,28,29]. The latter approach implies lower voltage of the battery system and thus lower cost of implementation, so it is more commonly encountered. In the grid-tie operation of such systems, the maximum power point (MPP) is either tracked by varying the direct axis component of the grid current vector, with the battery current being controlled by varying the ST duty ratio, as in [16–18,21], or the opposite is applied, as in [19,28]. In the island operation, the MPP can be tracked only by varying the ST duty ratio, whereas the battery current cannot be independently controlled [22,29].

Very few papers consider the qZSI as part of a SCIG-based WECS. Two of them are our previous studies [30,31]. The study presented in [30] offered only a simulation analysis of the system's performance and it lacked an extensive steady-state analysis with regard to system parameter variations. The study presented in [31] additionally included an experimental evaluation of the system's performance. It involved both transient and steady-state analysis, the system startup procedure, low-wind operation, responses to load and wind speed perturbations, and variations of the qZSI input and output voltages. Both these studies considered the WT and SCIG maximum power extraction, but they were both limited to island operation and did not include other renewable sources. A combination of the qZSI and a WT-driven SCIG was also considered in [32], where the SCIG was connected directly to the AC bus, along with the excitation capacitors, and used to power local loads. A static synchronous compensator consisting of a PV-fed qZSI with integrated batteries was connected to the same bus. The energy storage system additionally included a flywheel connected to the qZSI bridge input via a DC-DC converter. Still, the system in [32] cannot be considered a hybrid wind-solar power system in the full sense of the meaning because the WT-SCIG combination was the main power source in the system, whereas the PV subsystem was only used for power compensation. Finally, it did not include the possibility of optimizing the WT–SCIG power output and it was designed only for the island operation. The only paper to consider a hybrid wind-solar power system including both the battery-assisted qZSI and the SCIG-based WECS is our study reported in [33]. There the maximum power was extracted from both the PV and WECS, whereas the system's performance was experimentally evaluated over wide ranges of wind speed, solar irradiance, and load. However, battery charging control and grid-tie operation were not considered.

Since the ST state is not forbidden in the Z-source-type inverters, the dead time is generally omitted in the corresponding pulse-width-modulation (PWM) schemes [34,35]. However, as a result, unpredictable short-circuiting of the inverter bridge may occur in some cases due to non-ideal transistor switching dynamics. This leads to an unintended voltage boost and eventually to higher switching losses. By introducing the dead time of optimal duration in the sinusoidal PWM (SPWM) scheme, the qZSI efficiency can be increased by up to 11% and the electromagnetic interference reduced [36]. Additionally, by synchronizing the start of the ST state with the start of the zero-switching state and thus reducing the total number of switchings, the qZSI efficiency may be increased by as much as 4% [36].

The RES considered in this study is unique in terms of configuration and energy management. It is, in addition, the first wind-solar power system with the battery-assisted qZSI and the SCIG-based WT that is capable of both island and grid-tie operation. The

synergistic effect of the utilized primary level control algorithms that were developed as part of our previous studies is for the first time evaluated in this study. The power outputs of the WT, SCIG, and PV source are optimized through the application of the corresponding search-based algorithms. All the MPPT algorithms utilize the same input variable—the qZSI input power. In this way, the wind speed, the WT torque, the SCIG output power, and the PV current sensors are all omitted. The MPPT algorithms are executed in a successive manner, with the PV MPPT being prioritized due to higher rated power and faster dynamics. The SCIG is controlled by means of a speed-sensorless IRFO algorithm based on the advanced dynamic induction machine model, including the iron losses, the stray load losses (SLLs), and the magnetic saturation, which, in turn, allowed omission of the rotor speed sensor. The qZSI, acting as an interlinking converter between the DC bus and the AC grid/load, is controlled through the application of the SPWM scheme with dead time, in which the start of the ST state is synchronized with the start of the zero-switching state. The batteries are integrated into the qZSI to enable more efficient energy management, including the battery charging control. The performance of the proposed RES is evaluated through extensive experimental testing.

2. Configuration of the Proposed Wind–Solar System

The configuration of the considered hybrid wind-solar RES is shown in Figure 1. There are three main parts to the system: the wind energy subsystem (WES) (turquoise), the PV source (green)—both connected to the DC bus—and the battery-assisted qZSI (yellow) with the *LCL* filter at the output. The three-phase qZSI is either connected to the main grid or supplying an autonomous load. By setting the battery switch in Figure 1 to position 1, the batteries are connected directly to the DC bus. This is done only when both the solar and wind power are too low to ensure normal operation of the system (the batteries then act as the only power source) or when the PV source is not able to provide initial charging of the DC-bus capacitor (C_{dc}) (e.g., during nighttime). This capacitor not only acts as a DC voltage filter but also enables the initial magnetization of the SCIG. During normal operation of the system, the battery switch in Figure 1 is set to position 2, thus connecting the batteries in parallel with the capacitor C_2.

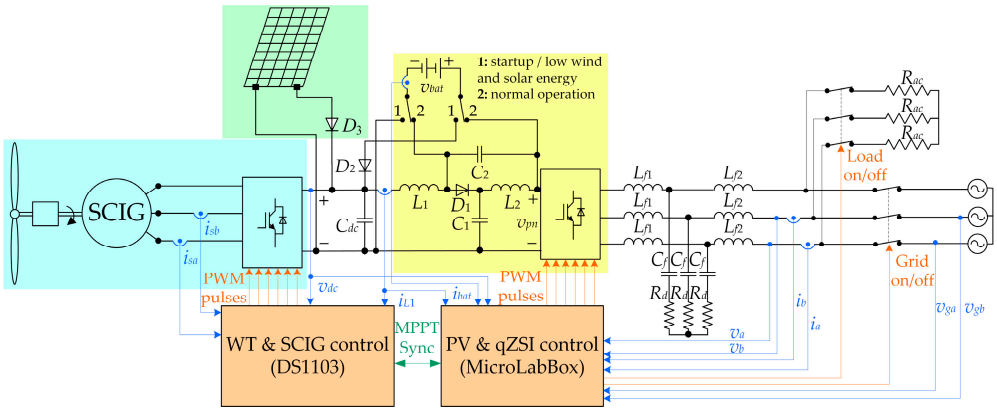

Figure 1. Configuration of the proposed qZSI-based wind–solar system.

It should be noted that the proposed control scheme requires a total of 11 sensors, with the corresponding signals denoted by blue lines in Figure 1. These are, namely, two AC currents at the SCIG output (i_{sa} and i_{sb}), a DC current and a DC voltage at the qZSI input (i_{L1} and v_{dc}), a DC battery current (i_{bat}), two AC currents and voltages at the *LCL* filter output (i_a and i_b; v_a and v_b), and two AC grid voltages (v_{ga} and v_{gb}). In this study, the control algorithms are executed in real-time by means of two distinct controllers (orange blocks in Figure 1): one dedicated to the WES control (DS1103) and the other a master controller covering the rest of the RES, including grid synchronization and load management (MicroLabBox). Figure 2 shows the corresponding block diagrams.

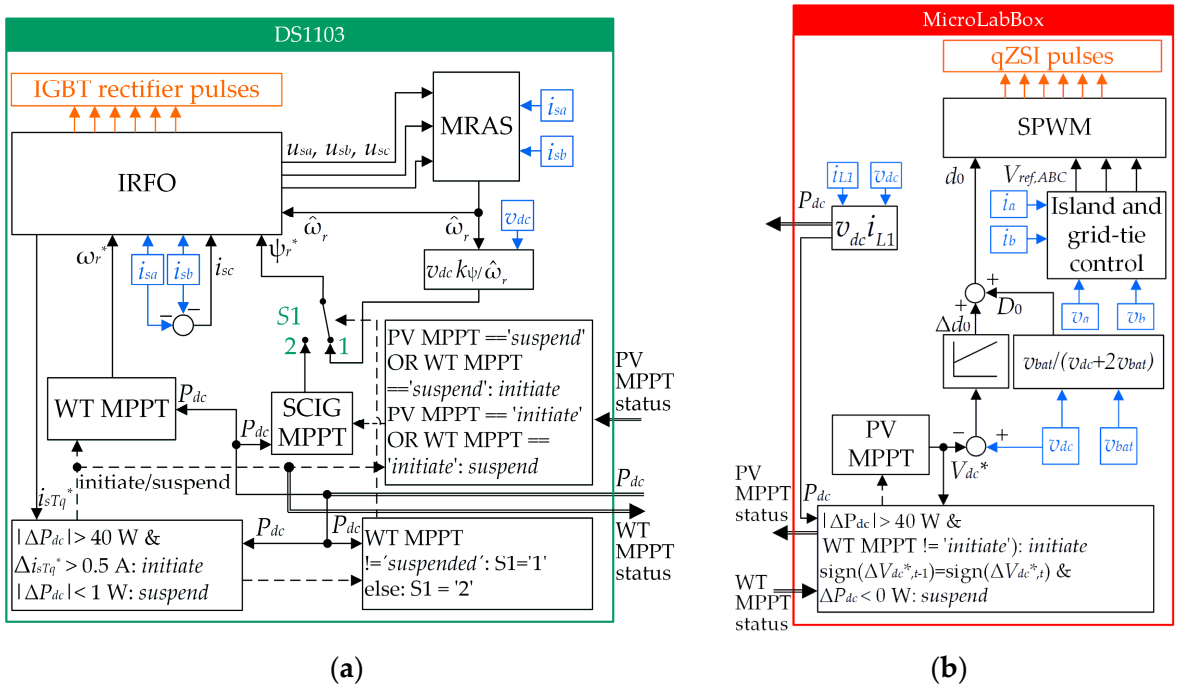

Figure 2. Proposed control algorithms: WT and SCIG control (**a**) and PV and qZSI control (**b**).

The operation of the two main controllers needs to be synchronized due to the successive execution of the MPPT algorithms, so they need to be able to communicate with each other ('MPPT Sync' in Figure 1). The details of the particular control algorithms which are relevant to particular segments of the RES are discussed below, starting with the WES.

2.1. Wind Energy Subsystem

2.1.1. Wind Turbine Characteristics

In this study, a variable-speed WT with a rated power of 1.5 kW and a rated wind speed of 11 m/s is considered. For any given wind speed within the normal operating range of the WT, the respective MPP can be reached through control of the WT rotational speed or torque. Since the WT shaft is coupled to the generator shaft through a step-up gearbox, the WT speed/torque control can be achieved through the generator speed/torque control. Figure 3 illustrates this concept by showing the mechanical power vs. rotor speed characteristics of the WT-driven SCIG utilized in this study, where the dashed line ($P_{m\text{-}max}$) represents the MPPs for different wind speeds. The SCIG is controlled by means of an IRFO algorithm, which allows for a decoupled control of the electromagnetic torque (i.e., the rotor speed) and the rotor magnetic flux. In this study, a search-based WT MPPT is implemented by utilizing an FL controller (FLC), as described in the next subsection.

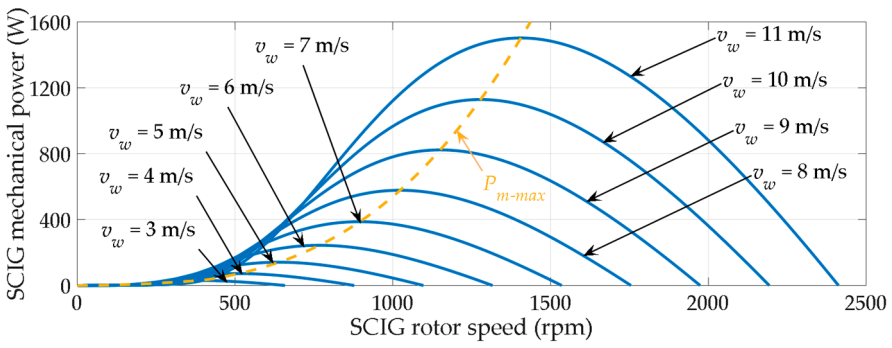

Figure 3. Mechanical power vs. rotor speed characteristics of the utilized WT-driven SCIG.

2.1.2. Maximum Wind Power Extraction

The proposed WT MPPT algorithm utilizes the qZSI input power (P_{dc}) as the input variable, as opposed to the SCIG mechanical power utilized in [31], and generates the rotor speed reference (ω^*_r) at its output. In this way, there is no need for the measurement or estimation of the SCIG torque. However, since the same input variable is utilized by all three MPPT algorithms, they need to be executed in a successive manner. In this case, this means that during the execution of the WT MPPT, two other MPPT algorithms—SCIG and PV—need to be suspended so that the P_{dc} variations could be undoubtedly attributed to the WT power variations, thus allowing the WT power trend to be correctly interpreted. The block diagram of the FL-based WT MPPT is shown in Figure 4. The reference speed is adjusted by $\Delta\omega^*_r$ based on the P_{dc} change and $\Delta\omega^*_r$ sign from the previous step. In this study, this adjustment is made every 1.5 s, which is enough time for the WT speed to stabilize between successive adjustments, thanks to the utilized HA speed controller.

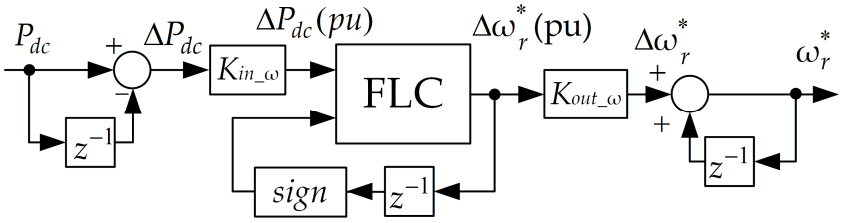

Figure 4. Block diagram of the FL-based WT MPPT algorithm.

Once the P_{dc} change recorded between two successive steps falls within ±1 W, the WT MPPT algorithm is suspended in order for the SCIG MPPT algorithm to take over (i.e., 'S1' in Figure 2a is moved to position '2'). The values of the input and output scaling factors (K_{in_ω} = 0.014, K_{out_ω} = 20) were derived by trial and error from simulation studies. The rule base for the FLC in Figure 4 is given in Table 1.

Table 1. Rule base for the fuzzy logic controller (FLC) in Figure 4. N, negative; P, positive; Z, zero; S, small; M, medium; B, big.

ΔP_{dc}	Sign ($\Delta\omega^*_r$)	
	N	**P**
PB	NB	PB
PM	NM	PM
PS	NS	PS
Z	Z	Z
NS	PS	NS
NM	PM	NM
NB	PB	NB

2.1.3. Speed-Sensorless IRFO Control

The IRFO algorithm implemented for the SCIG control is essentially the same as the one in [37], with only the online temperature correction of the SCIG equivalent resistances being left out for simplicity. The control algorithm is based on the advanced dynamic induction machine model, including the iron losses, the SLLs, and the magnetic saturation, proposed in [38]. The corresponding equivalent circuit is shown in Figure 5, whereas the corresponding differential equations can be found in [38].

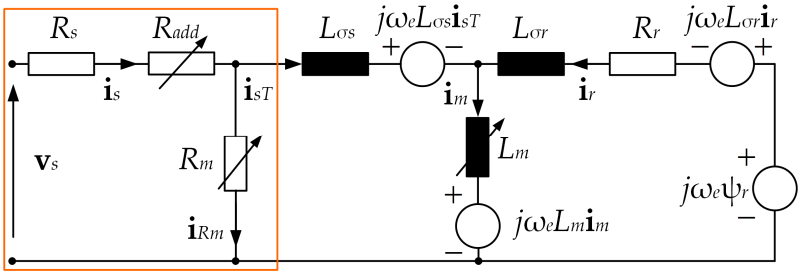

Figure 5. Space vector dynamic equivalent circuit of the SCIG model, including magnetic saturation and variable stray load and iron losses.

To simplify the equivalent circuit and equations, the variables and parameters within the rectangle in Figure 5 may be substituted with the Thevenin equivalents [38]

$$R_{sT} = \frac{(R_s + R_{add})R_m}{R_s + R_{add} + R_m} \tag{1}$$

$$\mathbf{v}_{sT} = \mathbf{v}_s \frac{R_m}{R_s + R_{add} + R_m} \tag{2}$$

$$\mathbf{i}_{sT} = \mathbf{i}_s \frac{R_s + R_{add} + R_m}{R_m} - \frac{\mathbf{v}_s}{R_m} \tag{3}$$

where R_s, R_{add} and R_m are the stator resistance, the SLL resistance, and the iron-loss resistance, respectively, whereas $\mathbf{v}_s$ and $\mathbf{i}_s$ denote the stator phase voltage and current space vectors, respectively.

The stator and rotor leakage inductances are considered constant and equal ($L_{\sigma r} = L_{\sigma s}$), whereas the main inductance (L_m) is considered variable with respect to the magnetizing current (I_m), as determined from the standard no-load test. The SLL and iron-loss resistances are defined as a function of the stator angular frequency (ω_e) and the rotor flux reference (ψ^*_r) as follows [38]:

$$R_{add} = R_{add,rated} \frac{\omega_e}{\omega_{e,rated}} \frac{\psi^*_r}{\psi_{r,rated}} \tag{4}$$

$$R_m = \frac{3\pi\omega_e}{K_h(\psi^*_r)} \tag{5}$$

where $K_h(\psi^*_r)$ denotes the flux-dependent iron-loss coefficient and $R_{add,rated}$ denotes the R_{add} value obtained from the standard variable-load test.

By utilizing a speed estimator instead of a physical speed sensor, the overall system cost is reduced and its reliability is increased. In this study, the speed is estimated by means of the model-reference adaptive system (MRAS), which is designed based on the previously described SCIG model. The corresponding block diagram is shown in Figure 6, in which pure integrators from (6) and (7) are replaced by first-order low-pass filters (T_f = 50 ms) to avoid problems related to the initial value and drift. The adaptive mechanism relies on the angular difference of the outputs of the reference and adaptive rotor flux estimators. The equations used for the calculation of the rotor-flux-linkage space vector from the so-called voltage (reference) and current (adaptive) models, respectively, are given as follows [38]:

$$s\hat{\boldsymbol{\psi}}_{rV} = \frac{L_r}{L_m}[\mathbf{v}_{sT} - (R_{sT} + \sigma L_s s)\mathbf{i}_{sT}] \tag{6}$$

$$s\hat{\boldsymbol{\psi}}_{rI} = \frac{L_m}{T_r}\mathbf{i}_{sT} - \left(\frac{1}{T_r} - j\hat{\omega}_r\right)\hat{\boldsymbol{\psi}}_{rI} \tag{7}$$

where ˆ denotes estimated quantities, bolded variables denote space vectors, symbol s stands for d/dt, and $_V$ and $_I$ denote the voltage (reference) and current (adaptive) models, respectively.

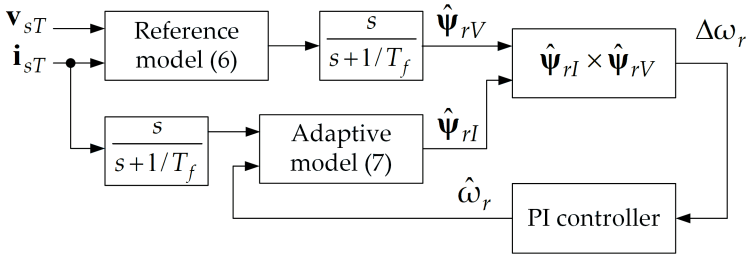

Figure 6. Block diagram of the MRAS-based speed estimation algorithm.

The block diagram of the speed-sensorless IRFO control algorithm implemented in this study is shown in Figure 7. There it can be seen that the reference value of the SCIG rotor angular speed (ω^*_r), generated by the WT MPPT algorithm, is compared with the corresponding estimated value ($\hat{\omega}_r$), generated by the MRAS. The speed error is then fed as an input signal to the HA controller, which, in turn, generates the reference value of the torque-related q-axis stator current at its output. The HA controller ensures fast response with practically no overshoot in the whole operating region and, hence, allows for a smaller time-step of the WT MPPT in comparison to the PI controller [7]. The reference value of the flux-related d-axis stator current is obtained by dividing the rotor flux reference (ψ^*_r) by the magnetizing inductance (L_m). The ψ^*_r value is, in turn, obtained at the output of the SCIG MPPT algorithm, which is discussed in the next subsection. The IRFO control algorithm also incorporates adaptive hysteresis control of the stator phase currents, with the hysteresis bandwidth set to 2% of the reference current amplitude [8]. Note that only two out of three stator phase currents need to be measured for this purpose because the SCIG stator windings are wye-connected with isolated neutral.

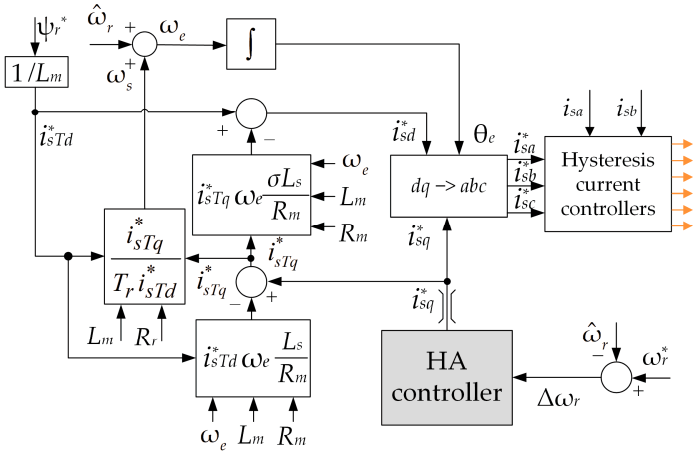

Figure 7. Block diagram of the speed-sensorless IRFO control algorithm.

2.1.4. Minimization of Generator Losses

The SCIG MPPT algorithm shown in Figure 8 shares the FL-based structure of the WT MPPT algorithm in Figure 4. The only difference is in the output variable (ψ^*_r) and the scaling factor values ($K_{in\_\psi} = 4.2/\omega_r$ and $K_{out\_\psi} = 1$, also derived by trial and error from simulation studies). The rule base for the FLC in Figure 8 is also identical to that in Table 1 provided that ω^*_r is substituted by ψ^*_r, whereas similar holds for the corresponding membership functions. The reader is referred to [8] for more details about the design and implementation of the WT and SCIG MPPT algorithms.

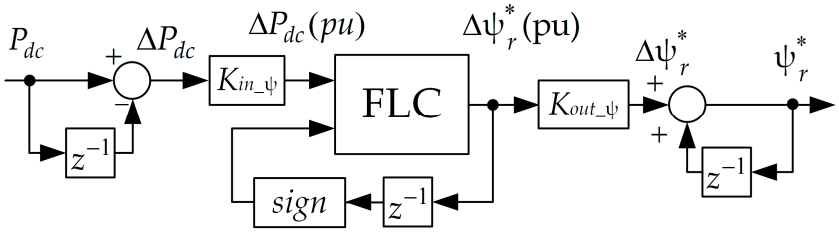

Figure 8. Block diagram of the FL-based SCIG MPPT algorithm.

It is well known that SCIG internal losses can be minimized through appropriate adjustment of the rotor flux while observing the effect of it on the output power. However, instead of measuring the SCIG output power or reconstructing it from the power converter switching pulses and the DC-bus voltage as in [31], the proposed SCIG MPPT algorithm utilizes the already available qZSI input power (P_{dc}) instead. In this study, the rotor flux adjustment is done every 1 s to account for the SCIG internal dynamics. The SCIG MPPT algorithm continues to operate until an abrupt change in the P_{dc} value is recorded (i.e., ΔP_{dc} > 40 W). In that case, it is first checked whether this change coincided with the abrupt change in the torque-related SCIG current (i_{sTq}). If this is the case, then this means that the wind speed has changed abruptly. Hence, the SCIG MPPT algorithm is deactivated, '*S*1' in Figure 2a is moved to position '1', and the WT MPPT algorithm is reinitiated. After the WT MPPT algorithm has converged, the SCIG MPPT algorithm is reinitiated and '*S*1' in Figure 2a is moved back to position '2'. Otherwise, if an abrupt change in the P_{dc} value did not coincide with the abrupt change in the i_{sTq} value, then this is interpreted as an abrupt change in solar irradiance. Consequently, the PV MPPT algorithm is reinitiated while suspending the SCIG MPPT (ψ^*_r is held at its current value). In this case, '*S*1' in Figure 2 is held in position '2'. After the PV MPPT algorithm has converged, the SCIG MPPT algorithm is reinitiated. It is reasonable to assume that the PV output power optimization does not affect the optimal WT speed, so there is no point in reinitiating the WT MPPT algorithm in this particular case.

2.2. Solar Energy Subsystem

2.2.1. Photovoltaic Source Characteristics

As it can be concluded from Figure 9, the power of a PV source varies with respect to both the solar irradiance (Z_1–Z_3) and panel temperature (T_1 and T_2). Still, for a specific value of these two parameters, there is an operating point where the PV source generates maximum power, and the task of the PV MPPT algorithm is to ensure that the PV source operates at the MPP for different environmental conditions. The movement of the MPP from OP_1 to OP_3 in Figure 9 is caused by the irradiance decrease ($Z_3 < Z_1$), whereas the movement from OP_1 to OP'_1 is caused by the temperature increase ($T_2 > T_1$). It is obvious that the MPP can be tracked through fine online tuning of the PV voltage (or current). In addition, the optimal value of the PV voltage is not significantly affected by the irradiance, so the MPP can be achieved over a wide range of irradiance levels by only slightly adjusting the PV voltage. Larger adjustments of this voltage are needed in the case of temperature variations.

2.2.2. Maximum Solar Power Extraction

The utilized P&O MPPT algorithm tracks the MPP by varying the PV source voltage, which is equal to the DC-bus voltage (v_{dc}), and it does so with the optimization time-step of 0.5 s. The principle of operation can be summarized as follows: if the PV voltage is perturbed in a given direction and the PV power increases as a result of this, then the PV voltage should be further perturbed in the same direction to move the operating point closer to the MPP; otherwise, the sign of the PV voltage perturbation has to be changed.

The MPP is achieved when there is no change in the PV power with respect to the PV voltage perturbations ($\Delta P_{pv}/V_{pv} = 0$). Mathematically, this control law is transcribed as

$$V_{pv}(k) = \begin{cases} V_{pv}(k-1) + V_{step}, & \frac{\Delta P_{pv}(k-1)}{\Delta V_{pv}(k-1)} > 0 \\ V_{pv}(k-1) - V_{step}, & \frac{\Delta P_{pv}(k-1)}{\Delta V_{pv}(k-1)} < 0 \end{cases} \quad (8)$$

where V_{step} denotes the voltage perturbation step and k denotes the execution step of the MPPT algorithm.

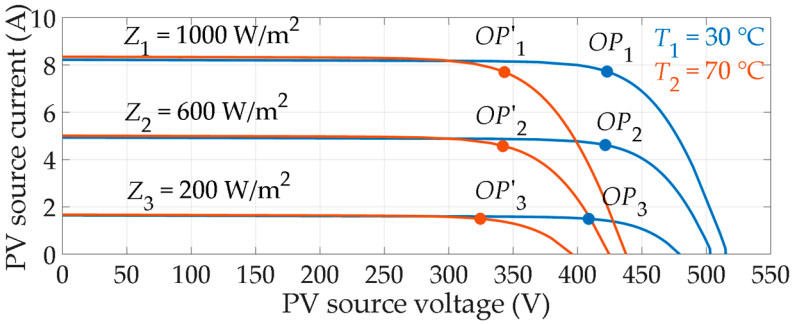

Figure 9. I-V characteristics of the utilized PV source.

In this study, the qZSI input power (P_{dc}) is utilized instead of the PV power (P_{pv}) in (8). The P_{dc} value is calculated as a product of the DC-bus voltage (v_{dc}) and the current flowing through L_1 (i_{L1}). Consequently, the proposed PV MPPT algorithm does not require the measurement of the PV source current. Note that the ΔP_{dc} value corresponds to the ΔP_{pv} value as long as the WT and SCIG MPPT algorithms are suspended.

Except during system startup, the considered PV MPPT algorithm is (re)initiated each time there is an abrupt change in the P_{dc} value that does not coincide with the abrupt change in the i_{sq} value, as explained before. Such behavior can be associated with a sudden change in solar irradiance, and in most cases, only a slight adjustment of the PV voltage is needed to reach the new MPP. Temperature changes are, on the other hand, much slower, so the PV power output needs to be reevaluated with regard to possible temperature variations on a much larger time scale. The PV MPPT could be, for example, reinitiated periodically every one or two hours in order to reevaluate the MPP position, but this feature is not considered in more detail in this paper. In the considered system, the actual PV voltage is varied through adjustment of the ST duty ratio of the qZSI. It is then compared to the corresponding reference value obtained at the output of the PV MPPT algorithm, whereas the error is fed into a dedicated PI controller.

2.3. Quasi-Z-Source Inverter with Batteries

2.3.1. Theoretical Background

The qZSI has one additional switching state compared to the conventional voltage-source inverters, which is known as the ST state. During this state, the transistors in the same inverter leg (one or all three legs, depending on the implemented PWM scheme) conduct, and the inductors L_1 and L_2 in Figure 1 deliver the previously accumulated energy to the capacitors C_1 and C_2, thus boosting the DC voltage level since the peak value of the voltage across the inverter bridge (V_{pn_peak}) is equal to the sum of the voltages across C_1 and C_2. Two equivalent circuits of the battery-assisted qZSI—one for the non-ST state and the other for the ST state—are shown in Figure 10a,b, respectively. R_{L1} and R_{L2} represent the parasitic resistances of the impedance network inductors, whereas the equivalent series resistance of the capacitors is neglected. In this study, the impedance network is considered to be symmetrical, i.e., $L_1 = L_2 = L$, $C_1 = C_2 = C$, $R_{L1} = R_{L2} = R_L$.

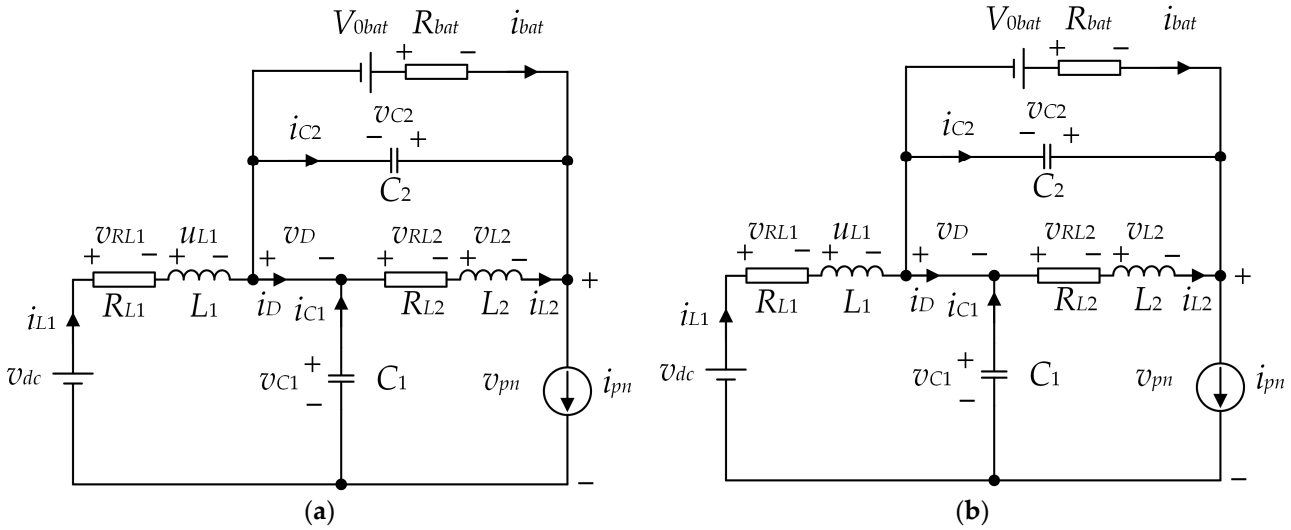

Figure 10. Equivalent circuits of the battery-assisted qZSI: non-ST state (**a**) and ST state (**b**).

The amount of the DC voltage boost depends on the ST duty ratio, i.e., the ratio of the ST state period (T_0) and the switching period (T). Consequently, the amplitude modulation index (M) and the ST duty ratio (D_0) of the qZSI can be utilized to achieve the required AC load voltage for any given value of the DC-bus voltage within the qZSI normal operating range. This is evident from the equations provided for the qZSI boost factor (B) and gain (G). The boost factor represents the ratio between the peak value of the voltage across the qZSI bridge (V_{pn_peak}) and the DC-bus voltage (V_{dc}), and it is given as

$$B = \frac{1}{1 - 2\frac{T_0}{T}} = \frac{1}{1 - 2D_0} \tag{9}$$

whereas the gain is defined as

$$G = \frac{V_{ac,\max}}{V_{dc}/2} = M \cdot B \tag{10}$$

where $V_{ac,\max}$ is the amplitude of the fundamental harmonic of the output phase voltage.

2.3.2. Zero-Sync Sinusoidal PWM with Dead Time

In this study, an SPWM scheme with injected third harmonic is implemented for the qZSI control. In addition, the start of the ST state is synchronized with the start of the zero-switching state so as to reduce the total number of switchings per transistor and, hence, reduce the switching losses. The desired duration of the ST state is achieved by utilizing the timer (LM555CN). The dead time (τ_d) of optimal duration is injected into the switching pattern so as to eliminate the unintended ST states, as explained before. The zero-sync SPWM scheme with dead time was first proposed in [36], where it was shown that the qZSI efficiency can be increased by more than 10% as a result of these actions. The corresponding waveforms of the reference voltages (v_{refA}, v_{refB}, v_{refC}), the carrier triangular signal (v_{trian}), the ST state signal (ST_{tim}), and the SPWM pulses of all the transistors (S_{A+}, S_{A-}, S_{B+}, S_{B-}, S_{C+}, S_{C-}) are shown in Figure 11. As noted in [36], it is important to set the τ_d value high enough to prevent the occurrence of the unintended ST states, but, at the same time, setting it too high can cause blocking of the diode in the qZSI impedance network and lead to higher distortion of the qZSI output voltage. In this study, the τ_d value was set to 0.7 µs, with the switching frequency set to f_{sw} = 5 kHz.

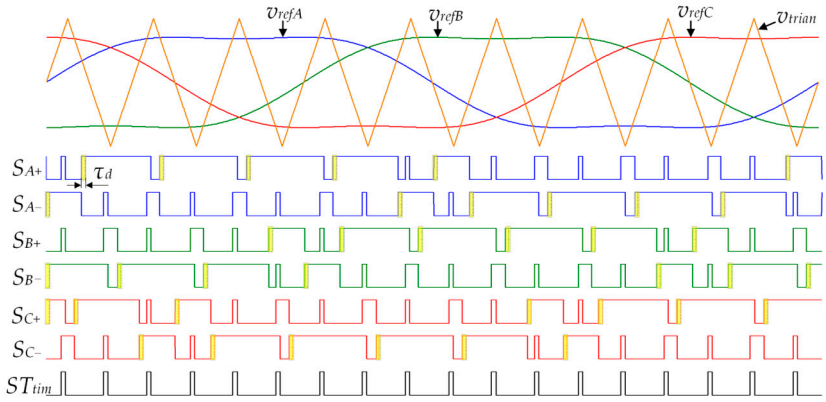

Figure 11. Waveforms of the utilized zero-sync SPWM with dead time (numerical simulation).

2.3.3. Battery Charging Control

In the island operation, the batteries are used to store all the excess energy generated by the WES and/or PV source or to provide compensation for the energy shortage. They also allow the system to operate for a limited period of time in conditions with no solar and wind power, as demonstrated in [31]. In the grid-tie operation, the batteries allow an additional degree of freedom in managing the energy injected into or taken from the grid, thus enabling medium- and long-term planning and accounting for certain economic aspects of the RES operation. In doing so, one has to monitor the batteries' state of charge in order to avoid them being overcharged or depleted. Further charging of the already charged batteries cannot be tolerated, so appropriate countermeasures must be taken. In the island operation, the battery current is not directly controlled, so the battery charging can be suspended only indirectly: by reducing the PV power output—e.g., by increasing the DC-bus voltage—and/or the WES power output—e.g., by speeding up the WT. Since both these variables are controlled in the considered RES, these actions can be easily taken if necessary. Similarly, further discharging of the already depleted batteries cannot be allowed, so in this case the energy consumption needs to be reduced—e.g., by disconnecting loads of lower priority or, as a last resort, by disconnecting all loads. In the grid-tie operation, the battery current is directly controlled (Figure 12), so the battery charging control comes down to setting the appropriate battery current reference.

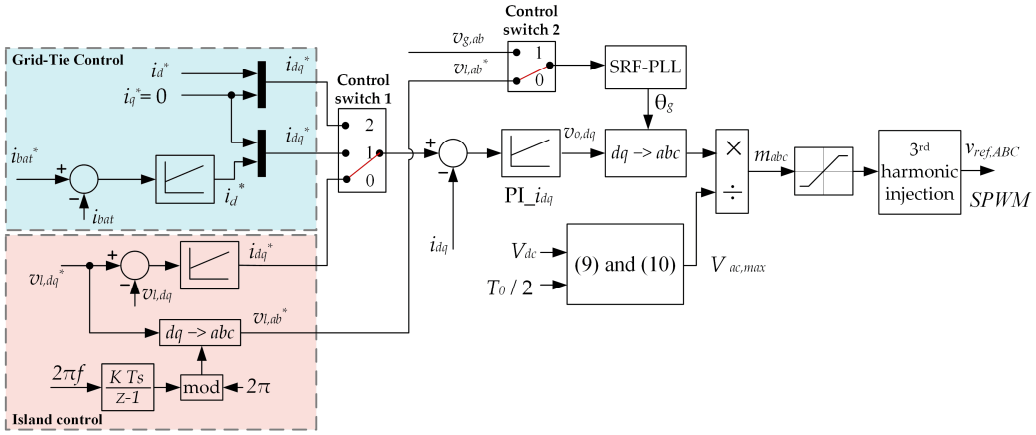

Figure 12. Block diagram of the grid-tie and island control algorithms.

2.4. Grid-Tie and Island Control Algorithms

The block diagram of the cascade-type grid-tie and island control algorithms is shown in Figure 12.

As it can be observed, in the grid-tie operation ('Control switch 1' in position '1' or '2' and 'Control switch 2' in position '1'), the synchronous reference frame phase-locked

loop (SRF-PLL) is used for the synchronization of the inverter output voltage with the grid voltage by maintaining $v_{od} = V_{g,\max}$ and $v_{oq} = 0$, where $V_{g,\max}$ is the amplitude of the grid phase voltage. At the same time, the system's angular frequency is set equal to that in the grid, where the angle θ required for the coordinate transformations is obtained as an integral of the angular frequency. By the implementation of the SRF-PLL, the active (p_{grid}) and reactive power (q_{grid}) injected into (or drawn from) the grid is defined as

$$\begin{aligned} p_{grid} &= \tfrac{3}{2} i_d V_{g,\max} \\ q_{grid} &= -\tfrac{3}{2} i_q V_{g,\max} \end{aligned} \tag{11}$$

Hence, p_{grid} is controlled by i_d, whereas q_{grid} is controlled by i_q. The d-axis current reference (i^*_d) is either obtained at the output of the battery current controller ('Control switch 1' in position '1') or set manually ('Control switch 1' in position '2'), whereas the q-axis current reference (i^*_q) is set to zero to achieve unity power factor at the point of common coupling.

In the island operation ('Control switch 1' in position '0' and 'Control switch 2' in position '0'), the d-axis voltage reference ($v^*_{l,d}$) is set to the desired amplitude of the fundamental component of the phase load voltage ($V_{l,\max} = 230 \cdot \sqrt{2}$). On the other hand, the q-axis voltage reference ($v^*_{l,q}$) is set to zero in order to ensure the load's active (p_{load}) and reactive power (q_{load}) to be defined as follows:

$$\begin{aligned} p_{load} &= \tfrac{3}{2} i_d V_{l,\max} \\ q_{load} &= -\tfrac{3}{2} i_q V_{l,\max} \end{aligned} \tag{12}$$

The angular frequency obtained by the SRF-PLL is in this case $\omega = 2\pi f_l$, where f_l is the desired fundamental frequency of the load voltage (f_l = 50 Hz in this study).

3. Experimental Setup

Figure 13 shows the laboratory setup used for the experimental evaluation of the proposed system. The main components are as follows:

1. DC power supply Chroma 62050H 600S programmed to emulate 16 series connected PV panels KC200GT (Kyocera)
2. Hall-effect transducers LA 50-P/S55 (SCIG currents), LA 55-P/SP52 (qZSI currents), DVL 500 (qZSI voltages), LV 25-P (load voltage), CV 3-500 (grid voltages) (LEM)
3. qZSI impedance network inductors with T520-26 (Micrometals) powder cores ($L_1 = L_2$ = 20.2 mH (unsaturated), R_L = 0.5 Ω (at 25 °C)), polypropylene capacitors MKSPI35-50U/1000 (Miflex) ($C_1 = C_2$ = 50 μF, ESR = 7.8 mΩ)
4. qZSI three-phase inverter bridge (IXBX75N170 IGBTs (IXYS) and SKHI 22B(R) drivers (Semikron)) with a switching frequency of 5 kHz
5. LCL filter at the qZSI output stage (L_{f1} = 8.64 mH, L_{f2} = 4.32 mH, C_f = 4 μF, R_d = 10 Ω)
6. MicroLabBox controller board (dSpace) for the qZSI control
7. Three-phase resistive load
8. Battery system with 20 lead–acid batteries (rated voltage 12 V, capacity 75 Ah)
9. Three-phase relay for load connection/disconnection
10. SCIG rated 1.5 kW (Končar, efficiency class IE1 [39])
11. DC motor rated 1.62 kW (SIEC) driven by SIMOREG DC-MASTER converter, type 6RA7031 (Siemens), used for WT emulation
12. Torque transducer TM 308 (Magtrol)
13. DS1103 controller board (dSpace) for the WT SCIG control
14. Incremental rotary encoder ROD 426 B (Heidenhain)
15. Three-phase IGBT bridge rectifier (SKM100GB125DN IGBT modules and SKHI 22B drivers (Semikron)) and DC-bus capacitor C_{dc} = 940 μF

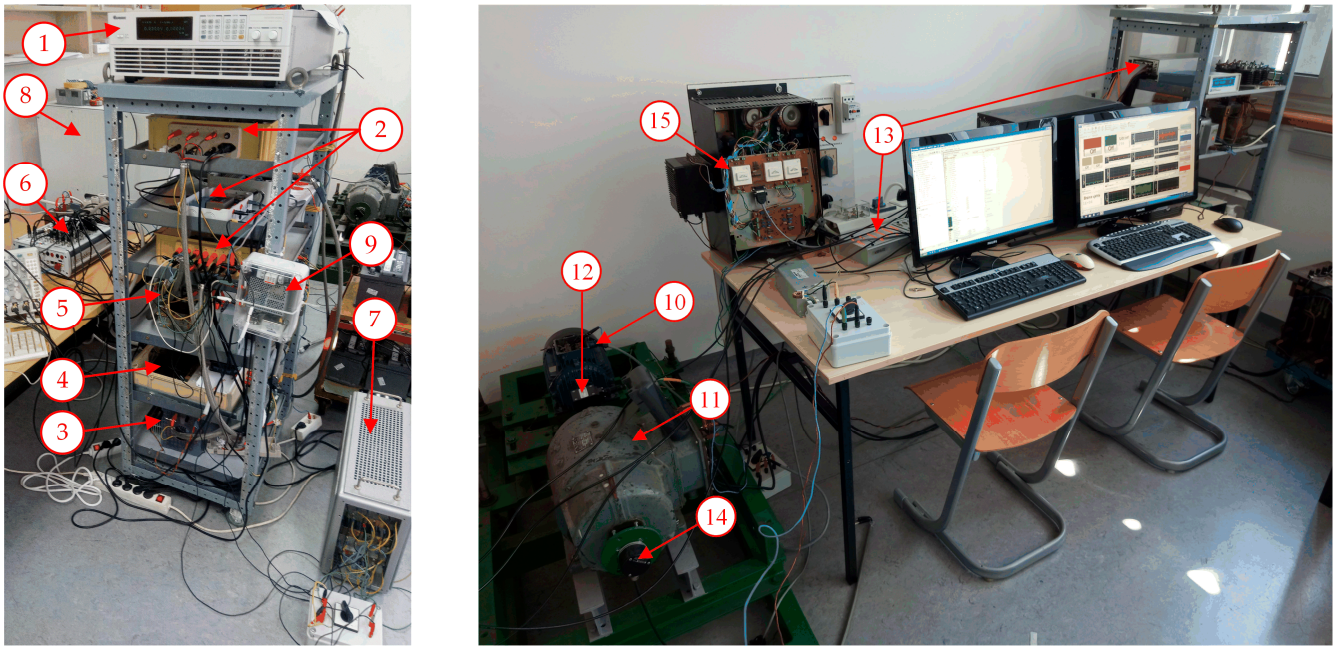

(**a**) (**b**)

Figure 13. Laboratory setup of the proposed system: (**a**) WES components; (**b**) qZSI and PV components.

4. Results and Discussion

To obtain an all-around performance analysis, the proposed system was evaluated through two experiments that included all considered upsets and perturbations, i.e., variations in wind speed, solar irradiance, and load. In the following sections, firstly the system's dynamic performance is evaluated in the island and grid-tie operation, after which the steady-state performance analysis is conducted.

4.1. Dynamic Performance

4.1.1. Island Operation

The dynamic performance of the system in island operation was evaluated based on the 250 s long experiment with the timeline shown in Figure 14 and the corresponding measured results shown in Figures 15 and 16.

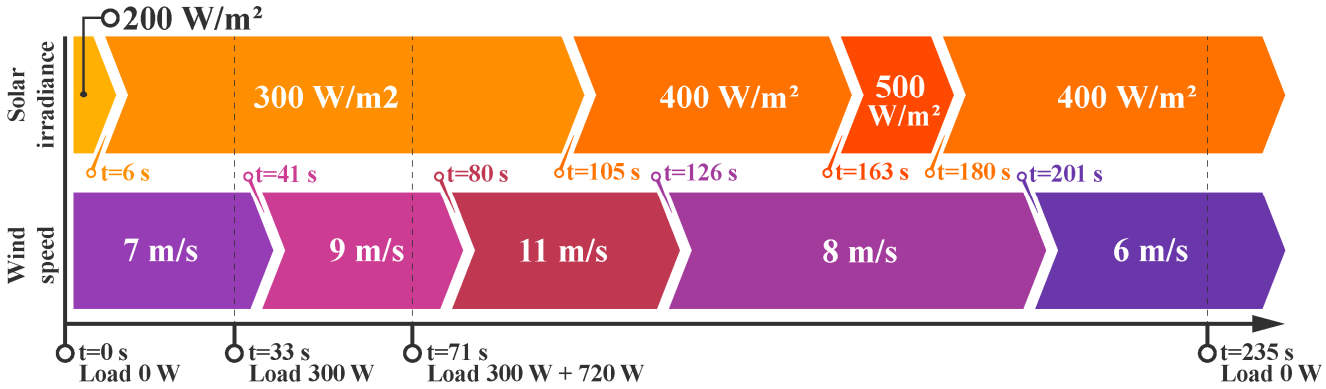

Figure 14. Timeline of events in the island operation experiment.

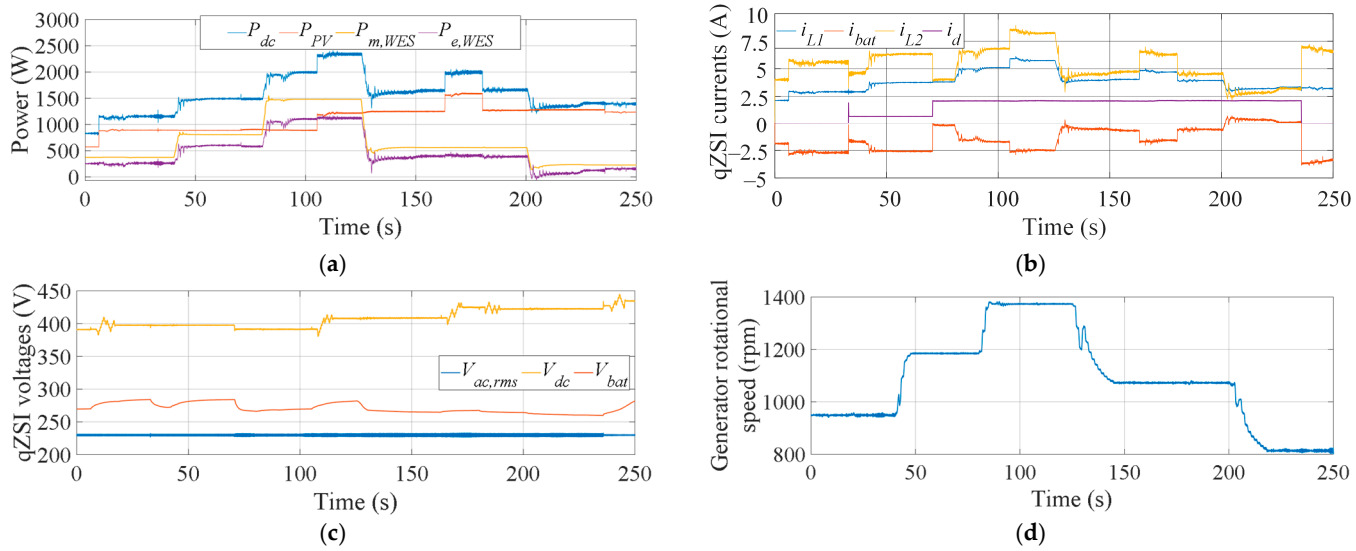

Figure 15. Dynamic responses during the island operation experiment: (**a**) electrical power and WT mechanical power; (**b**) qZSI currents; (**c**) qZSI voltages; (**d**) generator rotational speed.

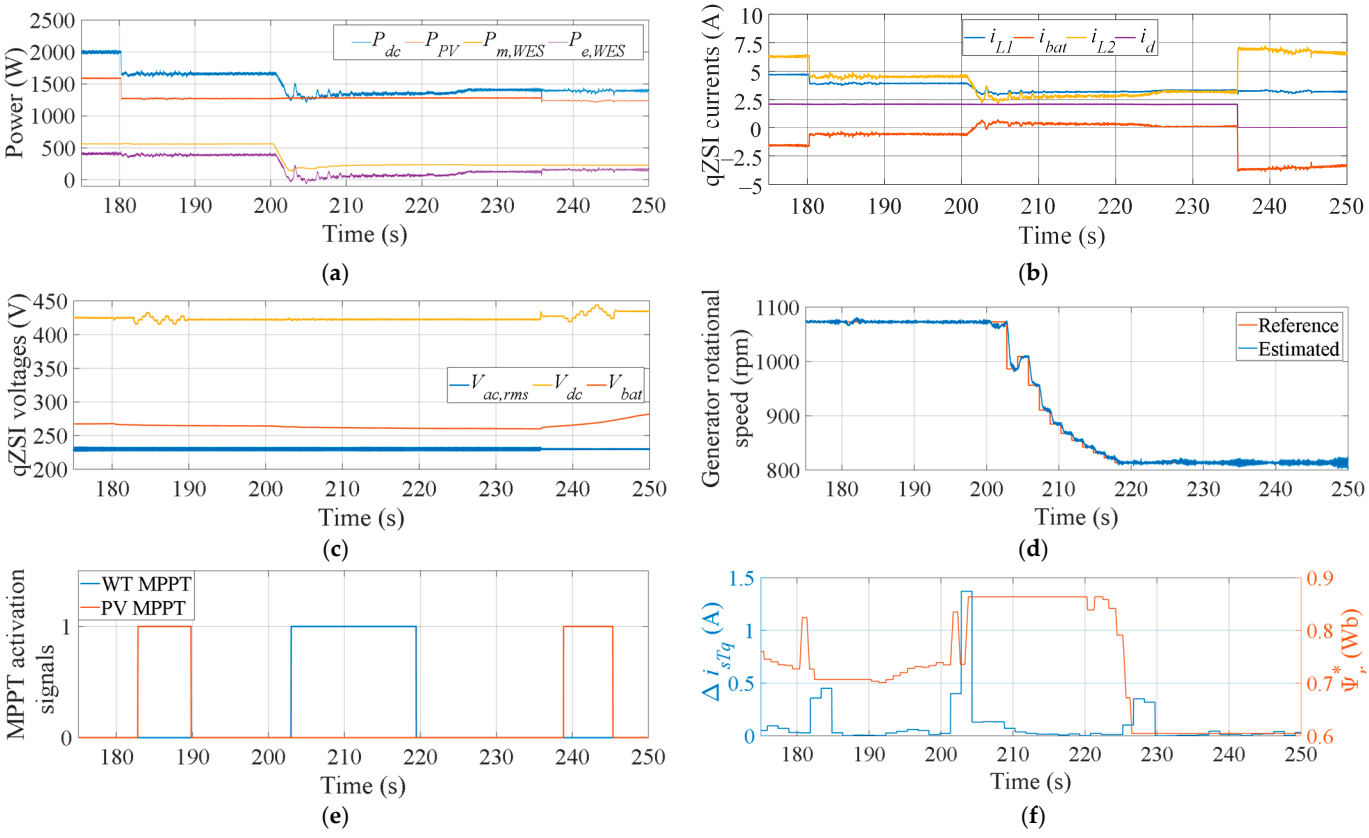

Figure 16. Dynamic responses to load, irradiance, and wind speed changes in the selected time interval (175–250 s): (**a**) electrical powers and WT mechanical power; (**b**) qZSI currents; (**c**) qZSI voltages; (**d**) generator rotational speed; (**e**) MPPT algorithms activation signals; (**f**) SCIG torque-related current change and rotor flux reference value.

The system was put into operation, and the optimization algorithms were activated prior to the initialization of the recording. The recording started in the steady-state operating point with a PV power output of ≈600 W and a WES power output of ≈250 W. Therefore, the total initial power output of the renewable sources was ≈850 W with no

loads connected at the output of the qZSI, so all the generated power (minus power losses) was routed into the batteries.

Figure 15 presents the experiment in its entirety to show how the system performed with regard to stability and robustness to disturbances, considering the main measured and controlled electrical variables.

Starting at $t \approx 6$ s, the solar irradiance increase from 200 W/m^2 to 300 W/m^2 resulted in the PV output power increase of 300 W (Figure 15a). The qZSI currents changed accordingly; namely, the current trough inductors L_1 and L_2 (i_{L1}, i_{L2}) increased while the battery current (i_{bat}) reached a greater negative value, indicating that even more energy is now stored in the batteries (Figure 15b). The direct component of the qZSI output current given in the synchronously rotating reference frame (i_d) did not change as there is no load connected at the output of the qZSI. The voltages shown in Figure 15c remain well under control, with the qZSI input bus voltage (V_{dc}) following the reference value provided by the PV MPPT algorithm, which will be analyzed in more detail later on. The battery voltage (V_{bat}) tends to increase due to charging, whereas the qZSI output AC voltage ($V_{ac,rms}$) remained at a given reference value of 230 V without any visible transients.

At $t \approx 33$ s, a three-phase resistive load of 300 W was connected at the qZSI output, which is mostly indicated by the change in the recorded currents. Expectedly, the steady-state value of i_d increased to ≈0.67 A, with the transient peak reaching ≈1.9 A. Similar transient peaks are also visible in i_{L2} and i_{bat}, while i_{L1} remained mostly undisturbed, as is the case with V_{dc} and $V_{ac,rms}$ as well. During the first two events of the experiment, both the WES output power and the generator rotational speed remained constant, showing that the observed disturbances did not affect the performance of the WES (Figure 15d).

The first wind speed change (from 7 m/s to 9 m/s) occurred at $t \approx 41$ s, resulting in an increase of ≈435 W and ≈355 W in the WT and SCIG output power, respectively, after reaching the optimal operating point. The wind speed change did not adversely affect other parts of the system, with the only visible changes in the qZSI currents due to the change in power balance.

An additional load of ≈720 W (i.e., ≈1020 W in total) was connected at $t \approx 71$ s. This disturbance did not generate any transient peaks in the recorded currents or in $V_{ac,rms}$, whereas the only visible change (i.e., decrease by ≈7 V) was observed in V_{dc}, despite being controlled by the dedicated controller. This is due to the measurement error induced by the increased ripple in the measured voltage used as the feedback signal.

Next, at $t \approx 80$ s, the wind speed changed again, this time from 9 m/s to 11 m/s. As a result, the WT and the SCIG output powers increased by ≈670 W and ≈520 W, respectively.

At $t \approx 105$ s, the solar irradiance increased to 400 W/m^2, resulting in PV output increase to ≈1220 W, so the total qZSI input power now reached ≈2345 W. With the connected load of ≈1020 W, the battery current reached −2.5 A, whereas the battery charging power reached ≈700 W ($V_{bat} \approx 280$ W). During this period, the qZSI output voltage remained under control.

The experiment continued with a wind speed decrease to 8 m/s at $t \approx 126$ s, which caused a significant drop in SCIG electrical power, reaching ≈100 W during transients, but eventually stabilized at ≈400 W without causing any deviations in the output voltage. It was followed by two consecutive solar irradiance changes, first to 500 W/m^2 ($t \approx 163$ s) and then back to 400 W/m^2 ($t \approx 180$ s), which also left the system undisturbed.

A final wind speed change down to 6 m/s resulted in the total qZSI input power dropping down to ≈1410 W. Although the load power was about 300 W lower, the batteries now began to discharge with a current of 0.13 A (i.e., ≈33 W) to compensate for the power losses in the system, whereas the qZSI output voltage once again remained under control.

Finally, at $t \approx 235$ s, both loads were disconnected simultaneously, and thus all surplus power was redirected to the batteries. Such sudden disconnection of loads did not cause any significant transient peaks, but it has positively affected the ripple in the measured voltages. As a consequence, the value of the V_{dc} feedback signal changed once again and falsely triggered the PV MPPT algorithm. However, this had no significant impact on the

performance of the system, causing minimal oscillations of the PV output power before returning to the optimal operating point.

Figure 16 provides a clearer insight into system performance—particularly the corresponding MPPT algorithms—during the period 175–250 s. At the start of the selected period, the system is in the steady-state operating point with the fixed V_{dc} and ω_r reference values, which are defined by the PV and WT optimization algorithms, respectively, for the given atmospheric conditions. Only the SCIG MPPT is active at that point and continuously tracks the maximum operating point of the SCIG.

The first change in the atmospheric conditions in the considered interval occurred at $t \approx 180$ s when the solar irradiance decreased from 500 W/m^2 to 400 W/m^2, resulting in a decrease of the qZSI input power by ≈320 W (Figure 16a). As explained earlier, both the PV and WT optimizations remain suspended and hold currently set V_{dc} and ω_r values until the system detects which of the renewable sources is responsible for the power change. The main control algorithm accomplishes this by observing the reference i_{sTq} current, which is proportional to the SCIG and WT torque (Figure 16f). If there is a significant change in the i_{sTq} value coinciding with the change in the qZSI input power between two WT optimization time-steps, it indicates a change in the WT output power (i.e., wind speed). This process takes at least one time-step, so the system holds previously obtained V_{dc} and ω_r values along with active SCIG optimization. As shown in Figure 16f, there is some change in the i_{sTq} current value at $t \approx 182$ s, but it is below the threshold value of 0.5 A, so the control algorithm detects the PV source as being responsible for the power change. Hence, the PV MPPT algorithm is reactivated at $t \approx 182$ s (Figure 16e) and the new optimal V_{dc} value is searched for, as seen in Figure 16c. Upon activation of the PV MPPT, the SCIG MPPT is suspended with the last obtained rotor flux reference held until it is reactivated again (Figure 16f). The V_{dc} value in Figure 16c oscillates around the new optimal value, which is obtained by averaging the V_{dc} value from the last 3 s. Next, the SCIG MPPT is reactivated, continuing from the last ψ^*_r value.

Regarding the significant changes in ψ^*_r and i_{sTq} values observed after the change in solar irradiance, they are interconnected and can be easily explained as follows: any change in solar irradiance directly affects the qZSI input power that changes accordingly, but considering that it is used as an input variable for all the considered MPPT algorithms, the currently active SCIG MPPT reacts to this change by adjusting the ψ^*_r value. A change in the ψ^*_r value affects the estimated generator speed (Figure 16d), which is estimated based on ψ^*_r, and since the estimated speed is used as a controller feedback signal, the controller reacts to this change by adjusting the i_{sTq} value. Since this behavior affects i_{sTq} only to some extent, it can be dealt with by setting the appropriate Δi_{sTq} threshold for the WT MPPT activation.

The next change in the atmospheric conditions occurred at $t \approx 200$ s when the wind speed decreased from 8 m/s to 6 m/s, resulting in a decrease of the WT output power (Figure 16a) as well as a SCIG speed drop below the reference value (Figure 16d). Again, the main control algorithm holds the PV and WT algorithms suspended until it determines the source of the power change. Meanwhile, the generator speed controller struggles to hold the rotor speed at the reference value by adjusting the i_{sTq} value, which, in turn, results in a significant Δi_{sTq} value. With the Δi_{sTq} value surpassing the set threshold of 0.5 A, the WT MPPT is immediately activated, whereas the SCIG MPPT is reset and suspended. This is confirmed by the WT MPPT activation signal in Figure 16e, which is also sent from the DS130 board to the MicrolabBox to prevent the false activation of the PV MPPT algorithm. With the WT MPPT algorithm reactivated, it searches for the new optimal rotor speed reference and reaches it at $t \approx 220$ s. Then, the SCIG MPPT is reactivated and in a few steps reaches the new optimal value $\psi^*_r = 0.605$ Wb (Figure 16f). This results in the SCIG output power increase of ≈60 W. During this time, the V_{dc} value remained undisturbed.

Note that an unexpected activation of the PV MPPT occurred at $t \approx 236$ s, caused by the disconnection of all loads, leading to a sudden change in the i_d, i_{bat}, and i_{L2} values. While disconnection of loads did not cause any significant transients in the measured

voltages, it affected the measurement noise level (Figure 16c), which ultimately caused a false detection of the input power change. Consequently, the PV MPPT algorithm was activated and a search for the new optimal V_{dc} value was initiated, but this event had no significant adverse effect on the overall system performance as the qZSI input power remained practically the same with only minimal temporary oscillations.

4.1.2. Grid-Tie Operation

A similar experiment as described above was conducted in the grid-tie operation, encompassing the same ranges of wind speed, solar irradiance, and load power, with the most significant difference being in the control approach. Because the system is connected to the grid, there is no need to control the output AC voltage as it is dictated by the grid. Therefore, only the output currents, defined in the synchronously rotating reference frame, are controlled, with i_d being proportional to the active output power and i_q being proportional to the reactive output power. During the entire experiment, the i_q reference value was set to zero to maintain zero reactive output power, while the i_d reference value was obtained as the output of the battery current controller. The battery current reference value was set to zero for the entire experiment, so all of the available power was routed to the local load and the grid.

Before the recording started, the system was synchronized and connected to the grid, with a local three-phase resistive load of 300 W connected. The system reached a stable steady-state operating point with the PV and WT power maximized and the SCIG MPPT active. The timeline of the entire experiment is shown in Figure 17, whereas the corresponding measured results are shown in Figures 18 and 19.

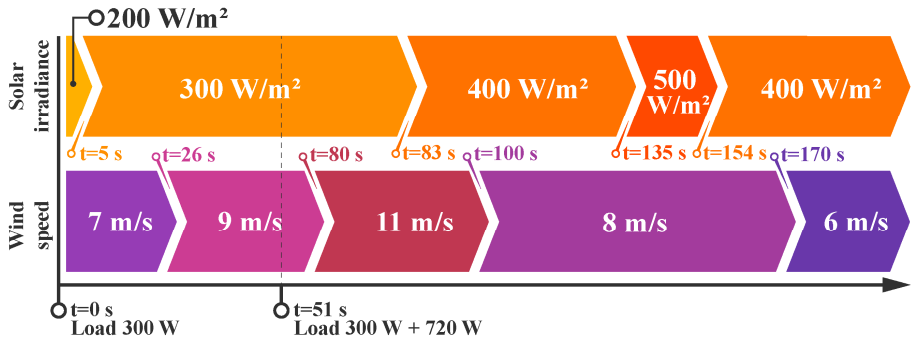

Figure 17. Timeline of events in the grid-tie operation experiment.

The obtained results testify to the good performance and stable operation of the system. The measured power values in Figure 18a responded accordingly to the changes in solar irradiance and wind speed, achieving the maximum power output from both the PV source and WT at different atmospheric conditions. Since the battery current was maintained at zero, i_{L1} was equal to i_{L2} (Figure 18b), which is in accordance with the qZSI equivalent circuit shown in Figure 9. The output current i_d was hence proportional to the qZSI input power and peaked at ≈3.58 A, which corresponds to ≈1845 W at the qZSI output. Wind speed changes did not cause any transient peaks in the observed variables, as opposed to solar irradiance changes, which did cause minor transient peaks (<1 A) in the battery current. This is expected as the qZSI power input changes due to solar irradiance variations were almost instantaneous. Connection and disconnection of loads, on the other hand, did not cause any visible transients except for some minor changes in the noise level of the measured $V_{ac,rms}$ signal. As can be seen in Figure 18c, the noise level of $V_{ac,rms}$ drops upon connection of the additional load at $t \approx 51$ s. This was partly reflected in the measured electrical powers but did not affect the performance of the system. Since the output current sensors are positioned before the load connection point, the system operation is not affected by the connected load in grid-tie operation: any shortage of power supply is covered by the grid, whereas surplus power is injected into the grid.

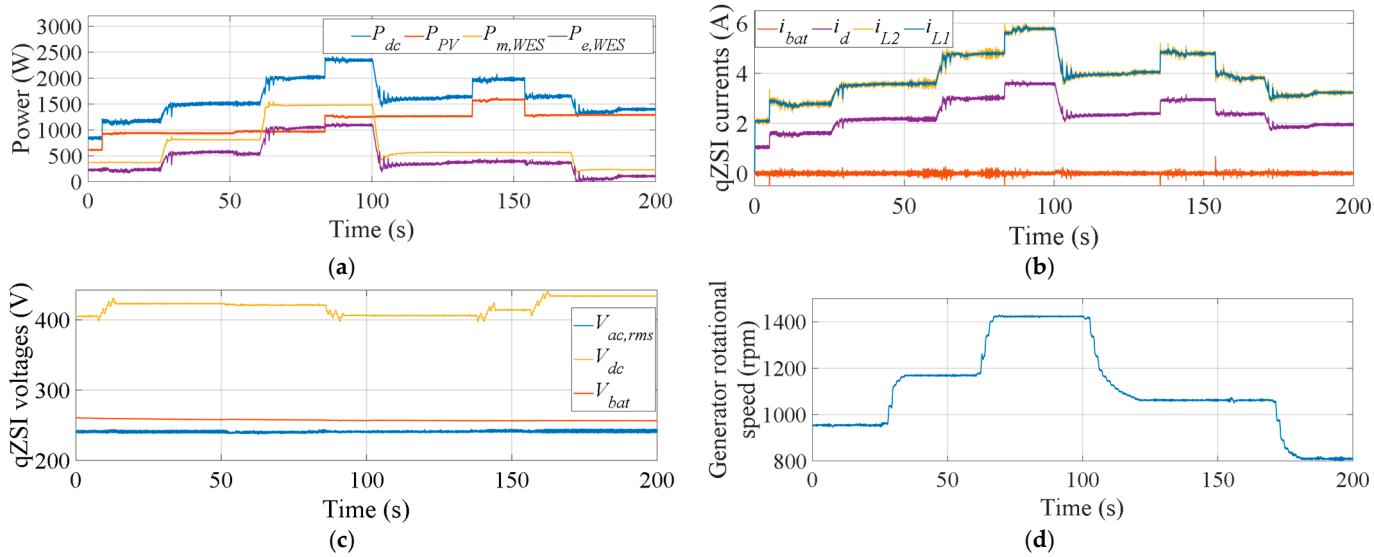

Figure 18. Dynamic responses during the grid-tie operation experiment: (**a**) electrical power and WT mechanical power; (**b**) qZSI currents; (**c**) qZSI voltages; (**d**) generator rotational speed.

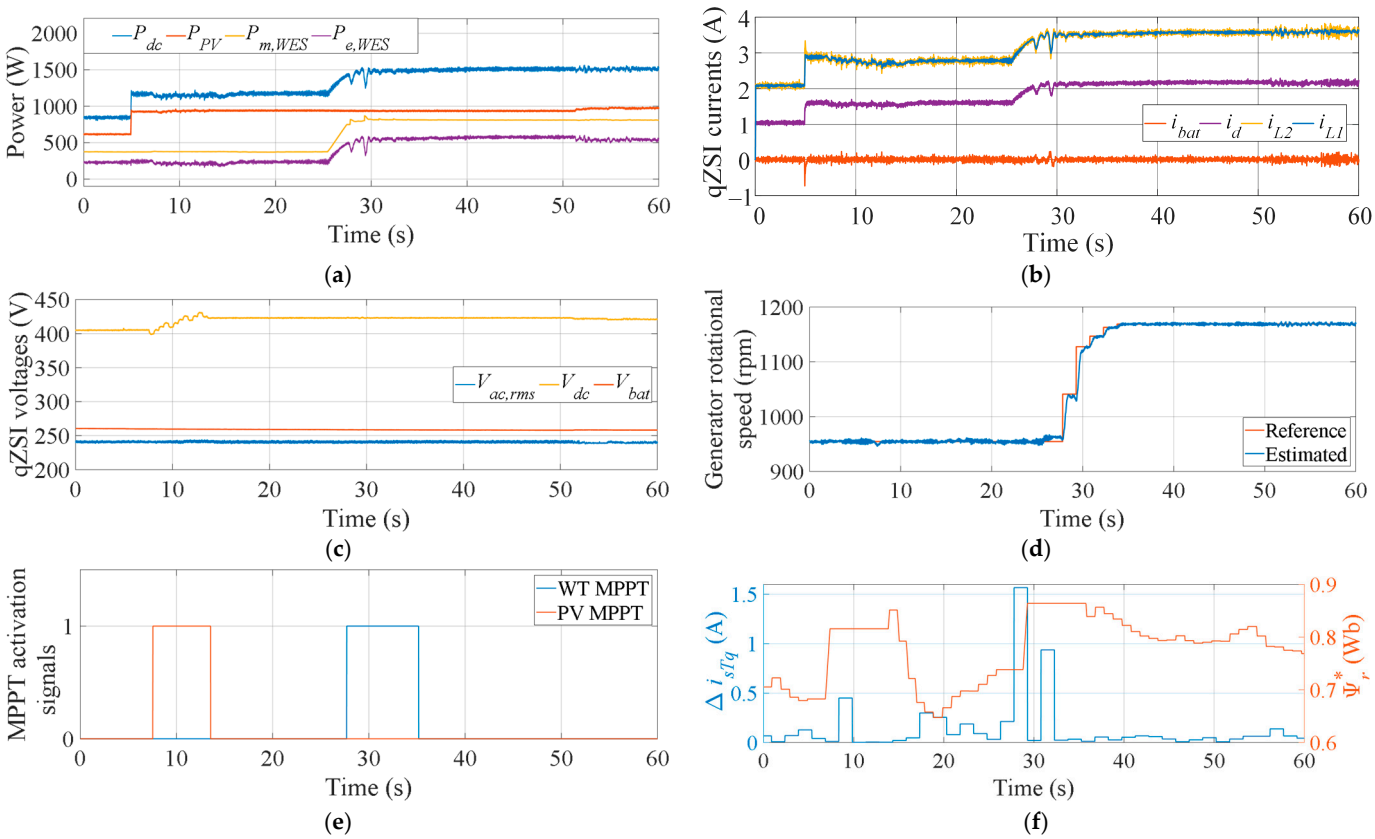

Figure 19. Dynamic responses to load, irradiance, and wind speed changes in the selected time interval (0–60 s): (**a**) electrical power and WT mechanical power; (**b**) qZSI currents; (**c**) qZSI voltages; (**d**) generator rotational speed; (**e**) MPPT algorithms activation signals; (**f**) SCIG torque-related current change and rotor flux reference value.

A clearer insight into system performance in grid-time mode—particularly the corresponding MPPT algorithms—is obtained by focusing on the selected time interval 0–60 s, shown in Figure 19. This interval includes a solar irradiance change, a wind speed change, and a change in load.

First, the solar irradiance change at $t \approx 5$ s led to an increase in the PV output power by ≈320 W (Figure 19a). There was a slight increase in Δi_{sTq} as well, but it was below the threshold of 0.5 A, so the PV MPPT was activated, whereas the SCIG MPPT was suspended. From Figure 19f it is obvious that the held value of ψ^*_r was significantly greater than the several preceding ψ^*_r values, which was due to the SCIG MPPT algorithm reacting to the $P_{in,qZSI}$ increase. It caused a minor drop in the WES output power (≈20 W), but it lasted less than 10 s, i.e., until the new optimal V_{dc} value was determined and the SCIG MPPT reactivated. There was no significant change in the V_{dc} value before and after the optimization (Figure 19c) because the solar irradiance changed by a relatively small margin, so the PV optimal power point did not move much with respect to the voltage. The solar irradiance change did, however, cause some transient peaks in the currents shown in Figure 19b, especially in the battery current. Still, note that such step changes in the solar irradiance are not realistic, but serve only for the purpose of testing.

Next, a wind speed change occurred at $t \approx 26$ s, which was recognized by the control algorithm through a distinctive increase in the Δi_{sTq} value. The WT MPPT was activated after a single time-step delay, as seen in Figure 19e, and the new optimal rotational speed was reached after only five perturbations.

Lastly, the additional load of 720 W was connected at $t \approx 51$ s. As explained earlier, the system operation in the grid-tie mode is practically unaffected by load perturbations except for the minor changes in the noise level of measured signals.

An additional experiment was performed to verify the battery charging control. During this experiment, the battery current reference was varied from 2 A to −2 A with a step of –0.25 A, whereas the atmospheric conditions were considered constant (i.e., solar irradiance of 400 W/m^2 and wind speed of 9 m/s), yielding constant output power from both the WES and PV source, and hence constant P_{dc} value, as shown in Figure 20a. The battery current closely tracked the respective reference, both in charging (negative i_{bat}) and discharging (positive i_{bat}) mode, whereas the d-axis component of the qZSI output current adapted correspondingly, as shown in Figure 20b.

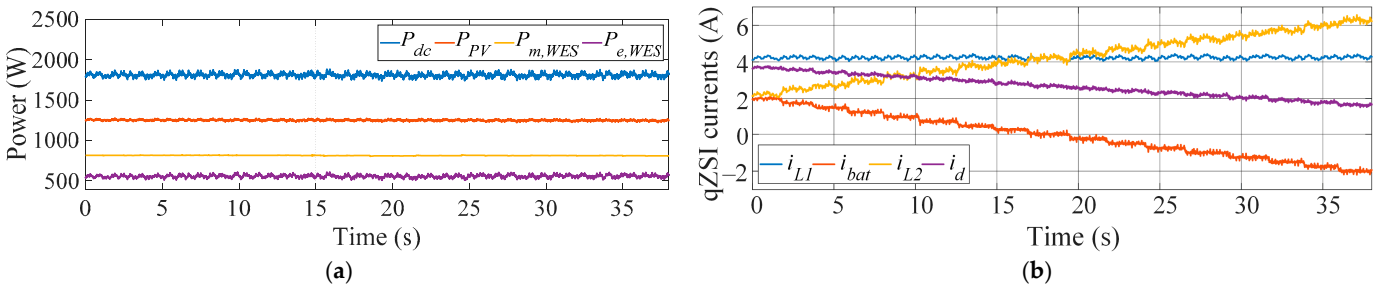

Figure 20. Dynamic responses to changes in the battery current reference: (**a**) electrical power and WT mechanical power, and (**b**) qZSI currents.

4.2. Steady-State Performance Analysis

To additionally evaluate the performance of the system, a steady-state analysis was conducted. Its goal was to determine the static tracking efficiency (STE) of the utilized MPPT algorithms as well as the system efficiency and power distribution. These results are shown in Figure 21.

The WT MPPT algorithm accuracy was evaluated based on the difference between the theoretical maximum values determined for the emulated WT and the achieved mechanical power values, measured at the generator shaft for different wind speeds. As is visible in Figure 21a, the offset decreases with increasing wind speed, reaching only around 1.5% at the rated wind speed of 11 m/s. These results were identical in the grid-tie and island operation. That was not the case with the PV MPPT algorithm, as can be observed in Figure 21b, but the maximum noted offset was still below 1.5%. To get a better sense of the accuracy of the MPPT algorithms, the results obtained in this study were compared to similar algorithms from the literature. For this comparison, mean offset values were

calculated for the data shown in Figure 21a,b, and then compared to the results of the PV and WT MPPT algorithms reported in [40–44]. The accuracy comparison is summarized in Table 2.

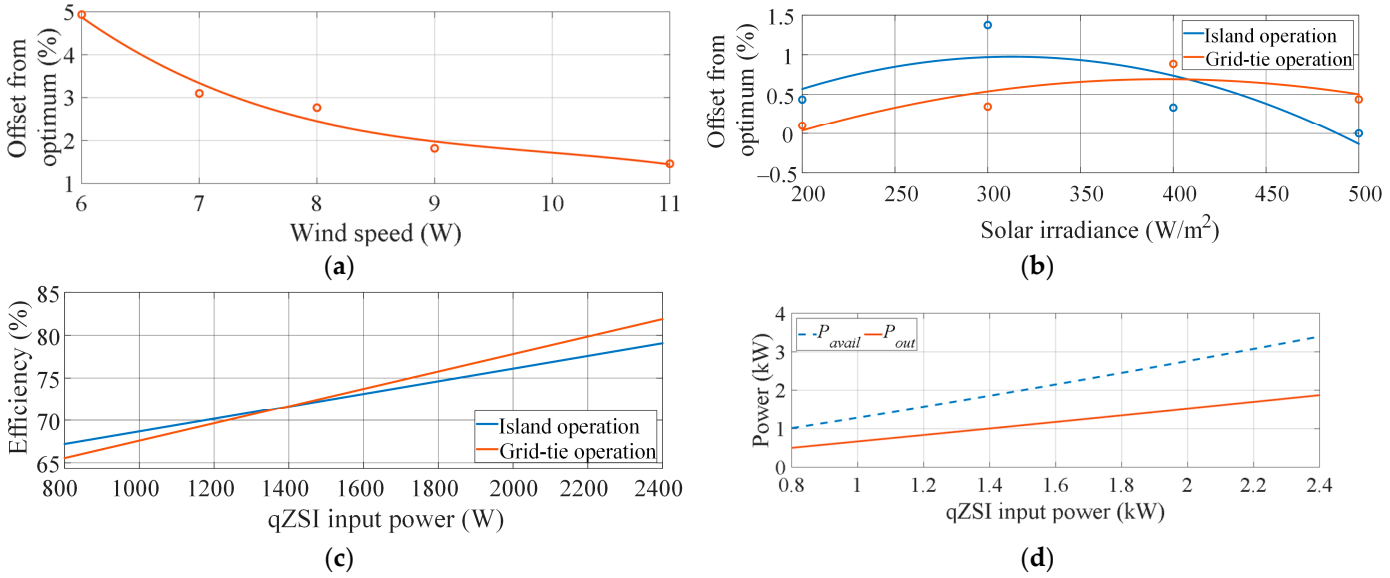

Figure 21. Steady-state characteristics depicting (**a**) WT MPPT accuracy vs. wind speed; (**b**) PV MPPT accuracy vs. solar irradiance; (**c**) qZSI efficiency vs. qZSI input power; (**d**) output power and available output power vs. qZSI input power.

Table 2. Comparison of MPPT accuracy.

	MPPT Type	WT MPPT Accuracy	PV MPPT Accuracy
This study	FL-suspended	97.18%	
[40]	Optimal torque control (OTC)	90.66%	
[40]	P&O (voltage)	87.94%	
[41]	P&O (duty-cycle)	99.57%	
[41]	Improved OTC	99.80%	
This study	P&O-suspended		99.51%
[42]	P&O		94.96%
[42]	FL		96.88%
[43]	Multi-FL		97.87%
[44]	Beta		97.6%
[44]	Incremental conductance		98.6%

The qZSI efficiency in Figure 21c was calculated as the ratio of the qZSI output power ± battery charging/discharging power and the qZSI input power for both grid-tie and island operation. The efficiency obviously increases with the input power because the share of the qZSI power losses drops. A somewhat steeper slope was obtained for the grid-tie operation. For the considered range of the input power, the qZSI efficiency ranged from about 65% to about 82%. Finally, Figure 21d shows the achieved output power (P_{out}) in the grid-tie operation, with the battery current set to zero. However, if one considers the additional power available potentially from the batteries, the total available output power (P_{avail}) is obtained. The latter term is calculated as the sum of P_{out} and the product of the battery voltage and the qZSI input current, which is the maximum battery discharging current. It can be observed in Figure 21d that the difference between P_{avail} and P_{out} increases with the qZSI input power, which is due to the increase of the qZSI input current and,

hence, the power available from the batteries. The total available output power reaches almost 3.5 kW for the qZSI input power of 2.4 kW.

Note that the maximum qZSI input power achieved in this study was 2.4 kW due to the technical limitations of the laboratory setup, whereas at the rated atmospheric conditions (i.e., solar irradiation of 1000 W/m^2, PV panel temperature of 25 °C, and wind speed of 11 m/s), the expected qZSI input power would be around 4.5 kW. Based on Figure 21c, at rated conditions, the efficiency of the qZSI would probably exceed 90%, whereas based on Figure 21d, the total available output power would probably exceed 6 kW.

5. Conclusions

In this paper, a hybrid wind-solar energy system was proposed, with the battery-assisted qZSI acting as an interlinking converter between the renewable energy sources and the utility grid—in grid-tie operation—or an autonomous load—in island operation. The maximum power extraction from renewable energy sources was ensured through the implementation of three dedicated MPPT algorithms. Both the dynamic and the steady-state performance of the proposed system was experimentally tested. It was shown that the system operates very well over a wide range of solar irradiance and wind speed values while ensuring maximum power extraction from the utilized power sources. The STE of the WT MPPT algorithm was between 95% for lower wind speeds and 98.5% for higher wind speeds, whereas the STE of the PV MPPT was above 98.5% in all the considered operating ranges. Furthermore, the output voltage and current controllers, used in the island and grid-tie operation, respectively, as well as the battery charging controller, performed satisfactorily, with no steady-state error regardless of sudden changes in weather conditions or loads connected to the AC bus, only with some minor transient peaks in the battery current of up to 0.7 A. This was all achieved while reducing the number of sensors required; namely, the SCIG rotational speed was estimated rather than measured, whereas the measurement of the WT torque, the SCIG output power, and the PV current was avoided because all three MPPT algorithms utilized the same input variable—the qZSI input power. The resulting overall cost reduction may reach several thousand euros and if one considers that small wind turbines (in a range of a few kW) can be bought for a fraction of that amount, such a cost reduction is by no means negligible. This, in turn, required effective coordination of the MPPT algorithms in the sense that each change in weather conditions is followed by a proper reaction of the corresponding MPPT algorithm. The integration of the battery system enabled more effective power flow management and increased the total available output power by up to 1.8 times.

The obvious disadvantage of the proposed control strategy is the inability to simultaneously track the MPP of different power sources, which is most pronounced when there is a significant simultaneous change in both solar irradiation and wind speed. However, such situations do not occur regularly. In the future, current MPPT algorithms are to be further improved and adapted to partial shading conditions, wind gusts, and higher-than-rated wind speeds.

Author Contributions: Conceptualization, M.B. (Matija Bubalo) and M.B. (Mateo Bašić); methodology, M.B. (Matija Bubalo), M.B. (Mateo Bašić), and I.G.; software, M.B. (Matija Bubalo), M.B. (Mateo Bašić), and I.G.; validation, M.B. (Matija Bubalo) and M.B. (Mateo Bašić); formal analysis, D.V.; investigation, M.B. (Matija Bubalo); resources, M.B. (Mateo Bašić) and D.V.; data curation, M.B. (Matija Bubalo); writing—original draft preparation, M.B. (Mateo Bašić) and M.B. (Matija Bubalo); writing—review and editing, M.B. (Mateo Bašić), M.B. (Matija Bubalo), I.G. and D.V.; visualization, M.B. (Matija Bubalo); supervision, M.B. (Mateo Bašić) and D.V.; project administration, D.V.; funding acquisition, M.B. (Mateo Bašić). All authors have read and agreed to the published version of the manuscript.

Funding: This research received no external funding.

Data Availability Statement: Not applicable.

Conflicts of Interest: The authors declare no conflict of interest.

References

1. Barakati, S.M.; Kazerani, M.; Aplevich, J.D. Maximum power tracking control for a wind turbine system including a matrix converter. *IEEE Trans. Energy Convers.* **2009**, *24*, 705–713. [CrossRef]
2. Sowmmiya, U.; Uma, G. Control and maximum power tracking operation of hybrid excited variable speed induction generator. *Electr. Power Syst. Res.* **2017**, *143*, 771–781. [CrossRef]
3. Hong, C.M.; Cheng, F.S.; Chen, C.H. Optimal control for variable-speed wind generation systems using General Regression Neural Network. *Int. J. Electr. Power Energy Syst.* **2014**, *60*, 14–23. [CrossRef]
4. Chen, C.H.; Hong, C.M.; Cheng, F.S. Intelligent speed sensorless maximum power point tracking control for wind generation system. *Int. J. Electr. Power Energy Syst.* **2012**, *42*, 399–407. [CrossRef]
5. Nayanar, V.; Kumaresan, N.; Gounden, N.A. A single-sensor-based MPPT controller for wind-driven induction generators supplying dc microgrid. *IEEE Trans. Power Electron.* **2016**, *31*, 1161–1172. [CrossRef]
6. Mesemanolis, A.; Mademlis, C.; Kioskeridis, I. High-efficiency control for a wind energy conversion system with induction generator. *IEEE Trans. Energy Convers.* **2012**, *27*, 958–967. [CrossRef]
7. Vukadinović, D.; Bašić, M.; Nguyen, C.H.; Nguyen, T.D.; Vu, N.L.; Grgić, I. Hedge-Algebra Speed Controller—Experimental Implementation in a Sensorless Stand-Alone WECS. In Proceedings of the 2020 International Symposium on Industrial Electronics and Applications, Banja Luka, Bosnia and Herzegovina, 4–6 November 2020. [CrossRef]
8. Bašić, M.; Vukadinović, D.; Grgić, I.; Bubalo, M. Energy efficient control of a stand-alone wind energy conversion system with AC current harmonics compensation. *Control Eng. Pract.* **2019**, *93*, 104185. [CrossRef]
9. Simoes, M.G.; Bose, B.K.; Spiegel, R.J. Design and performance evaluation of a fuzzy-logic-based variable-speed wind generation system. *IEEE Trans. Ind. Appl.* **1997**, *33*, 956–965. [CrossRef]
10. Senjyu, T.; Ochi, Y.; Kikunaga, Y.; Tokudome, M.; Yona, A.; Muhando, E.B.; Urasaki, N.; Funabashi, T. Sensor-less maximum power point tracking control for wind generation system with squirrel cage induction generator. *Renew. Energy* **2009**, *34*, 994–999. [CrossRef]
11. Errouissi, R.; Al-Durra, A.; Muyeen, S.M. A robust continuous-time MPC of a DC–DC boost converter interfaced with a grid-connected photovoltaic system. *IEEE J. Photovolt.* **2016**, *6*, 1619–1629. [CrossRef]
12. Jain, C.; Singh, B. A three-phase grid tied SPV system with adaptive DC link voltage for CPI voltage variations. *IEEE Trans. Sustain. Energy* **2016**, *7*, 337–344. [CrossRef]
13. Anderson, J.; Peng, F.Z. Four Quasi-Z-source Inverters. In Proceedings of the 2008 IEEE Power Electronics Specialists Conference, Rhodes, Greece, 15–19 June 2008. [CrossRef]
14. Babaa, S.E.; Armstrong, M.; Pickert, V. Overview of maximum power point tracking control methods for PV systems. *J. Power Energy Eng.* **2014**, *2*, 59–72. [CrossRef]
15. Eltawil, M.A.; Zhao, Z. MPPT techniques for photovoltaic applications. *Renew. Sustain. Energy Rev.* **2013**, *25*, 793–813. [CrossRef]
16. Liu, Y.; Ge, B.; Abu-Rub, H.; Iqbal, A.; Peng, F. Modeling and Controller Design of Quasi-Z-Source Inverter with Battery Based Photovoltaic Power System. In Proceedings of the 2012 IEEE Energy Conversion Congress and Exposition, Raleigh, NC, USA, 15–20 September 2012. [CrossRef]
17. Liu, Y.; Ge, B.; Abu-Rub, H.; Peng, F.Z. Control system design of battery-assisted quasi-z-source inverter for grid-tie photovoltaic power generation. *IEEE Trans. Sustain. Energy* **2013**, *4*, 994–1001. [CrossRef]
18. Liu, Y.; Ge, B.; Abu-Rub, H.; Peng, F.Z. Modelling and controller design of quasi-Z-source inverter with battery-based photovoltaic power system. *IET Power Electron.* **2014**, *7*, 1665–1674. [CrossRef]
19. Sun, D.; Ge, B.; Bi, D.; Peng, F.Z. Analysis and control of quasi-Z source inverter with battery for grid-connected PV system. *Int. J. Electr. Power Energy Syst.* **2013**, *46*, 234–240. [CrossRef]
20. Sun, D.; Ge, B.; Peng, F.Z.; Rub, H.A.; Almeida, A.T.D. Power Flow Control for Quasi-Z Source Inverter with Battery Based PV Power Generation System. In Proceedings of the 2011 IEEE Energy Conversion Congress and Exposition, Phoenix, AZ, USA, 17–22 September 2011. [CrossRef]
21. De Oliveira-Assis, L.; Soares-Ramos, E.P.P.; Sarrias-Mena, R.; García-Triviño, P.; González-Rivera, E.; Sánchez-Sainz, H.; LlorensIborra, F.; Fernández-Ramírez, L.M. Simplified model of battery energy-stored quasi-Z-source inverter-based photovoltaic power plant with Twofold energy management system. *Energy* **2021**, *244*, 122563. [CrossRef]
22. Abu-Rub, H.; Iqbal, A.; Ahmed, S.M.; Peng, F.Z.; Li, Y.; Baoming, G. Quasi-Z-source inverter-based photovoltaic generation system with maximum power tracking control using ANFIS. *IEEE Trans. Sustain. Energy* **2013**, *4*, 11–20. [CrossRef]
23. Grgić, I.; Bašić, M.; Vukadinović, D.; Bubalo, M. Fixed-Duty-Cycle Control of a Quasi-Z-Source Inverter in a Battery-Assisted Photovoltaic System. In Proceedings of the 2019 20th International Symposium on Power Electronics, Novi Sad, Serbia, 23–26 October 2019. [CrossRef]
24. Monjo, L.; Sainz, L.; Mesas, J.J.; Pedra, J. State-space model of quasi-z-source inverter-PV systems for transient dynamics studies and network stability assessment. *Energies* **2021**, *14*, 4150. [CrossRef]
25. Monjo, L.; Sainz, L.; Mesas, J.J.; Pedra, J. Quasi-Z-source inverter-based photovoltaic power system modeling for grid stability studies. *Energies* **2021**, *14*, 508. [CrossRef]
26. Ge, B.; Abu-Rub, H.; Peng, F.Z.; Lei, Q.; Almeida, A.T.d.; Ferreira, F.J.T.E.; Sun, D.; Liu, Y. An energy-stored quasi-z-source inverter for application to photovoltaic power system. *IEEE Trans. Ind. Electron.* **2013**, *60*, 4468–4481. [CrossRef]

27. Ge, B.; Peng, F.Z.; Abu-Rub, H.; Ferreira, F.J.T.E.; de Almeida, A.T. Novel energy stored single-stage photovoltaic power system with constant DC-link peak voltage. *IEEE Trans. Sustain. Energy* **2014**, *5*, 28–36. [CrossRef]
28. Khajesalehi, J.; Sheshyekani, K.; Hamzeh, M.; Afjei, E. High-performance hybrid photovoltaic-battery system based on quasi-Zsource inverter: Application in microgrids. *IET Gener. Transm. Distrib.* **2015**, *9*, 895–902. [CrossRef]
29. Li, F.; Ge, B.; Sun, D.; Bi, D.; Peng, F.Z.; Abu-Rub, H. Quasi-Z-Source Inverter with Battery Based PV Power Generation System. In Proceedings of the 2011 International Conference on Electrical Machines and Systems, Beijing, China, 20–23 August 2011. [CrossRef]
30. Bubalo, M.; Bašić, M.; Vukadinović, D.; Grgić, I. Optimized Isolated Operation of a WECS-Powered Microgrid with a Battery-Assisted qZSI. In Proceedings of the 6th International Conference on Electric Power and Energy Conversion Systems, Istanbul, Turkey, 5–7 October 2020. [CrossRef]
31. Bubalo, M.; Bašić, M.; Vukadinović, D.; Grgić, I. Experimental investigation of a standalone wind energy system with a battery-assisted quasi-Z-source inverter. *Energies* **2021**, *14*, 1665. [CrossRef]
32. Ramachandran, S.; Ramasamy, M. Solar photovoltaic interfaced quasi impedance source network based static compensator for voltage and frequency control in the wind energy system. *J. Electr. Eng. Technol.* **2021**, *16*, 1253–1272. [CrossRef]
33. Grgić, I.; Bašić, M.; Vukadinović, D.; Bubalo, M. Optimal Control of a Standalone Wind-Solar-Battery Power System with a Quasi-Z-Source Inverter. In Proceedings of the 2020 9th International Conference on Renewable Energy Research and Application, Glasgow, UK, 27–30 September 2020. [CrossRef]
34. Babaei, E.; Abu-Rub, H.; Suryawanshi, H.M. Z-source converters: Topologies, modulation techniques, and application–part I. *IEEE Trans. Ind. Electron.* **2018**, *65*, 5092–5095. [CrossRef]
35. Vijayan, V.; Ashok, S. Hybrid control for bidirectional Z-source inverter for locomotives. *Adv. Power Electron.* **2015**, *2015*, 264374. [CrossRef]
36. Grgić, I.; Vukadinović, D.; Bašić, M.; Bubalo, M. Efficiency boost of a quasi-Z-source inverter: A novel shoot-through injection method with dead-time. *Energies* **2021**, *14*, 4216. [CrossRef]
37. Bašić, M.; Bubalo, M.; Vukadinović, D.; Grgić, I. Sensorless maximum power control of a stand-alone squirrel-cage induction generator driven by a variable-speed wind turbine. *J. Electr. Eng. Technol.* **2021**, *16*, 333–347. [CrossRef]
38. Bašić, M.; Vukadinović, D. Small-size induction machine equivalent circuit including variable stray load and iron losses. *J. Electr. Eng. Technol.* **2018**, *13*, 1604–1613. [CrossRef]
39. *IEC 60034-30-1*; Rotating Electrical Machines—Part 30-1: Efficiency Classes of Line Operated AC Motors. IEC: Geneva, Switzerland, 2014.
40. Abdullah, M.A.; Yatim, A.H.M.; Tan, C.W.; Saidur, R. A review of maximum power point tracking algorithms for wind energy systems. *Renew. Sustain. Energy Rev.* **2012**, *16*, 3220–3227. [CrossRef]
41. Zhang, X.; Jia, J.; Zheng, L.; Yi, W.; Zhang, Z. Maximum power point tracking algorithms for wind power generation system: Review, comparison and analysis. *Energy Sci. Eng.* **2023**, *11*, 430–444. [CrossRef]
42. Devarakonda, A.K.; Karuppiah, N.; Selvaraj, T.; Balachandran, P.K.; Shanmugasundaram, R.; Senjyu, T. A comparative analysis of maximum power point techniques for solar photovoltaic systems. *Energies* **2022**, *15*, 8776. [CrossRef]
43. Rajesh, R.; Mabel, M.C. Efficiency analysis of a multi-fuzzy logic controller for the determination of operating points in a PV system. *Sol. Energy* **2014**, *99*, 77–87. [CrossRef]
44. Brito, M.A.G.; Galotto, L.; Sampaio, L.P.; Melo, G.A.; Canesin, C.A. Evaluation of the main MPPT techniques for photovoltaic applications. *IEEE Trans. Ind. Electron.* **2013**, *60*, 1156–1167. [CrossRef]